Image processing and noise reduction techniques for thermographic images from large-scale industrial fires

by J. de Vries*

* FM Global, Research Division, Norwood, MA 020062 USA. Jaap.devries@fmglobal.com

Abstract

In this study, the effectiveness of extending an uncooled fixed-integration-time IR camera's temperature range via a reduced aperture was shown and applied to thermographic analysis of large-scale industrial fires. The increase in noise equivalence temperature difference (NETD) caused by extending the temperature range of the camera was quantified and a Kalman and a median noise filtering algorithm were proposed. Results show that both an Adaptive Kalman Filter (AKF) and an Adaptive Median Filter (AMF) can reduce the low temperature image noise by 55% and 62% respectively.

1. Introduction

In a typical rack-storage fire test scenario, fire development consists of ignition followed by a period of vertical and horizontal fire growth. After application of water, either via sprinklers or other water delivery methods, a significant development of smoke and steam can ultimately obscure part (or all) of the test array. This buildup of smoke and steam significantly affects visual observations. An example image sequence taken using a regular video camera is shown in figure 1.
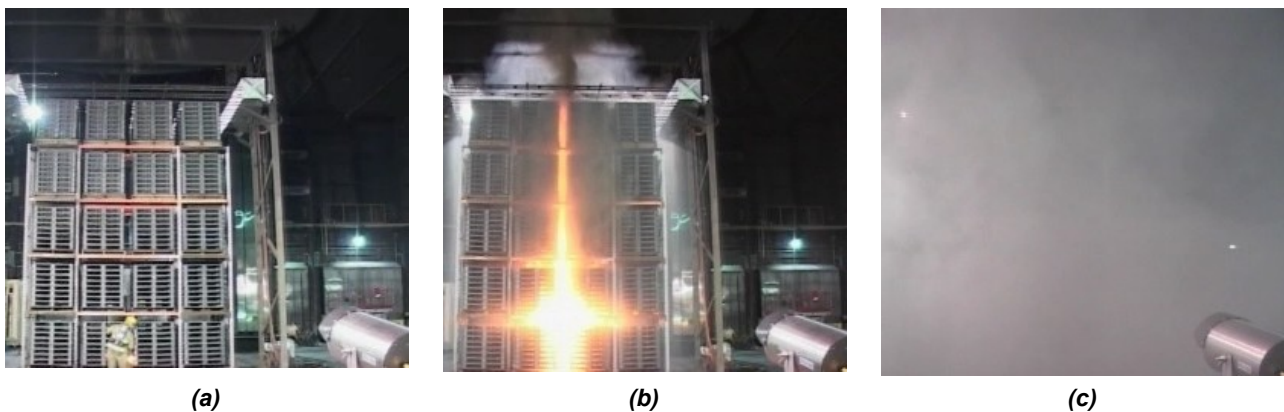

(a) *(b)* *(c)*

Fig. 1. *Image sequence of a fire test underneath a water application apparatus located at FM Global's Research Campus with images taken at: ignition at time zero (a), fire development after 3 minutes (b), complete obstruction of the array by the smoke and steam after 5 minutes (c).*

The fire in figure 1 involves plastic pallets. The visible images clearly show the ignition and fire growth during the early stages of the test; however, after water is applied, significant build-up of smoke and steam starts blocking the view of the array. Five minutes after ignition, the view is completely obscured and the fuel array is no longer visible. At this point, visual observation of the fire is no longer possible. This can be of particular concern when one of the pass/fail criteria of the test is based on whether the fire is capable of reaching a certain location, such as the end of the array. In addition, decisions regarding test termination often have to be made based on fire development, which further emphasizes the importance of fire observation.

The ability of an IR camera to see through gases, small particles and small droplets can greatly enhance the visibility during a fire test. For example, figure 2 shows a 640 x 480 long-wave infrared (LWIR) image registered on top of a full 1080p visible (*i.e.,* Vis) video frame. The gray colors surrounding the IR frame actually represent smoke and steam and clearly show the level of obscuration during this test. Significant digital image and video processing techniques are required for this procedure before the two images can be registered [1]. Both the LWIR and Vis frames are corrected for non-linear lens distortions (barrel distortion) caused by using wide angle lenses. Also, both frames are corrected for perspective distortion, allowing images to be registered when taken from different angles. Figure 2 clearly shows the merits of using IR thermography when studying large-scale fire phenomena.
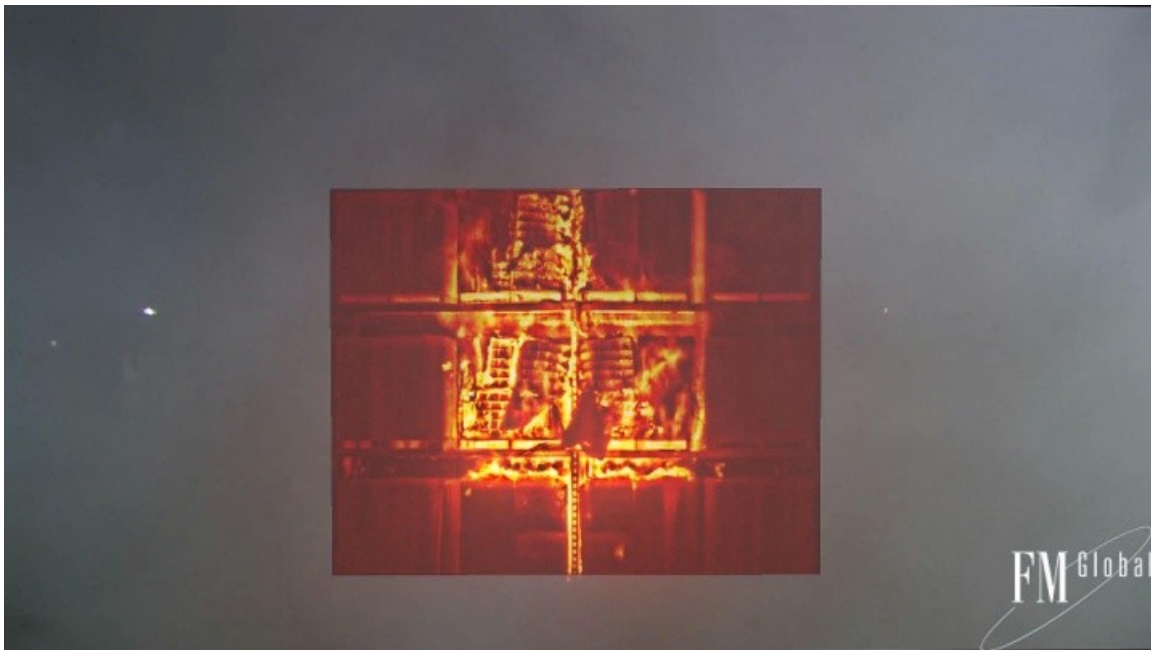
Fig. 2. *LWIR image registered on top of a Vis HD video frame; streaks from water flow can be observed.*

Currently FM Global has two IR cameras available to study fire phenomena; namely the FLIR® SC7600 ORION Indium Antimonide (InSb) photon detector and the FLIR® SC655 microbolometer camera. Several prior studies using these cameras were performed and are reported in references [2]-[5].

Microbolometer detectors have the following two disadvantages when compared to the mid-wave Indium Antimonide photon detector: First, the integration time is longer. A microbolometer camera has a time constant ~10 ms; therefore, 50 ms is required to collect 99% of the signal measurement. By comparison, an InSb photon detector has a time constant in the order of micro or even nano seconds. In addition, the Noise Equivalent Temperature Difference (NETD) can be up to three times higher [6].

With respect to the slow response time, for industrial fires, the fire growth rate and plume frequencies are typically low. For example, when dealing with pool fires Zukoski [7] suggested that the plume frequency is primarily a function of the pool diameter so that

$$f = (0.50 \pm 0.04)\sqrt{\frac{g}{D}} \ Hz. \tag{1}$$

In Eq. (1), *f* represents the plume's oscillating frequency, *g* is the gravitational constant (9.81 *m/s²*), and *D* is the diameter of the pool fire. In many practical cases the dominant frequency is on the order of 1 Hz. Therefore, studying fire phenomena using infrared themography allows for slower IR systems as opposed to, for instance, thermoelastic stress analysis (TSA) [6]. While Eq. (1) was derived for pool fires specifically, many of the industrial fires studied inside FM Global's Large Burn Laboratory have frequencies on the order of 1 Hz or less. Therefore, the relative long integration time of the microbolometer camera poses little practical concerns.

While the response time and noise characteristics of a microbolometer camera are inferior when compared to those of a typical photon detector, the cost benefit of microbolometer cameras - five to ten times less expensive that their InSb counterparts - make them a popular choice. Another benefit of microbolometer cameras is the ability to see through smoke and small water droplets due to their long wave sensitivity. The purpose of this study is to demonstrate the usefulness of a microbolometer camera when studying industrial (warehouse) fires in a laboratory setting. Of particular interest in this study is to double a microbolometer camera's temperature range while approximately maintaining its original (factory) noise characteristics. The latter objective will be achieved by utilizing adaptive noise filtering.

2. Camera system used

2.1. Camera specifications

All infrared images were acquired using an uncooled FLIR® SC655 microbolometer [8]. This camera has a 640x480-pixel uncooled microbolometer thermal detector with a (17 μm) pixel resolution sensitive at wavelengths between 7.5 μm and 13 μm. The field of view (FOV) of the lens is 25º x 18.8º, providing a 0.69 mrad spatial resolution. The maximum (full) frame rate of this camera is ~40 Hz. The SC655 LWIR camera has a factory pre-calibrated object

temperature range of -20ºC to 150ºC or 0ºC to 650ºC with an accuracy of ±2ºC or ±2%, whichever is greater. The camera's focus and temperature range can be set remotely using the control and analysis software accompanying the camera (Thermovision® ExaminIR). The integration times are fixed and cannot be modified by the operator. The long-wave spectral range of the FLIR® SC655 makes it possible to look through smoke and small sized particles and droplets.

When exposed to temperatures exceeding the camera's range, a pixel will saturate and no more information can be obtained. Sensor saturation can be prevented by attenuating the incoming signal by either placing a reduced size aperture or a neutral density (ND) filter in front of the lens. While saturation may be suppressed, in many cases factory-calibrated relationship between raw signal and surface temperature will no longer be applicable. To regain calibrated temperature information, the thermographer will either have to send the camera back for an extended factory calibration (costly and time consuming) or perform the calibration him or herself using a –preferably NIST traced- blackbody radiant source (also costly and labor intensive).

A third option is to calibrate the camera while in use (in-situ) by exposing it to an attenuated and subsequently un-attenuated quasi-steady temperature scene. This method was described in detail by the author in a previous publication [2]. However, for completeness, a short synopsis of the method and its results are presented next.

2.1. Temperature extension and in-situ calibration

The in-situ calibration allows an extension of the camera's usable temperature range and, when using a reduced aperture, increasing the depth of field (increasing F-number). The incoming IR signal is attenuated via a fixed diameter aperture, which consists of a plastic lens cap with a 12.7 mm through hole. During the in-situ calibration, thermographic images with and without the aperture are taken in rapid succession (40 fps) and compared. The assumption (and prerequisite) is that the temperature field is at a quasi-steady state and there is sufficient dynamic range of temperatures within the scene to allow for calibration. An example of the aperture used in this study is shown in figure 3. The raw pixel signal with and without the aperture present were sorted and are plotted against each other in figure 4. Noticeably, saturation is observed when the un-attenuated raw signal, Φ_{NA}, reaches the maximum of $2^{16} - 1$ (65535) digital counts. The portion of the signal in which there is no saturation can be correlated (black dashed line in figure 4). This correlation can be used to record temperatures up to 1200ºC. The calibrated temperature as function of attenuated (aperture present) digital raw counts is slightly non-linear and given by the following equation:

$$T(\Phi_A) = 3.415 \cdot \sqrt{(6.336E - 5 \cdot \Phi_A^2 + 2.949 \cdot \Phi_A - 22229.5)} - 26.78 \tag{2}$$

In Eq. (2), Φ_A is the raw attenuated signal count and T is the temperature in ºC. The attenuated signal causes the absolute noise levels to increase, which is particularly noticeable in the low temperature regime. Characterizing and mitigating this noise will be discussed next.

Fig. 3. *Reduced aperture used in present study, foil was used to protect the camera from any incoming radiant heat transfer.*
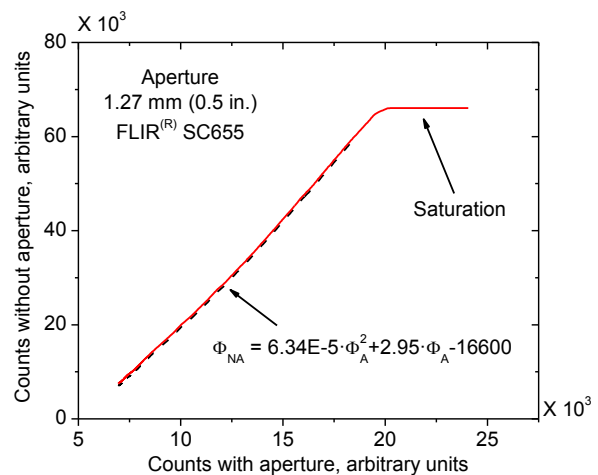

Fig. 4. *Sorted attenuated raw signal plotted against un-attenuated raw signal. Pixel saturation of the full signal noticeable at 65535 counts.*

2.2. Noise equivalent temperature difference (NETD)

Due to the change of the signal transfer function with the object temperature, the NETD decreases with increasing object temperature [9]. The effect of temperature on the noise equivalent temperature difference was obtained using a blackbody radiant source (Infrared Systems Development model# 564/301, 20ºC to 1200ºC) powered by an

IR-301 blackbody controller. The results of NETDs obtained are shown in Table 1. The method for obtaining the NETD was described by the author previously [2]. Briefly, for each blackbody temperature setting (ranging between 0 and 1200ºC), a point measurement was taken at ~40 fps for 1000 frames. The NETD was determined by estimating the standard deviation of the point measurement over 1000 frames. A similar method was described by Vollmer et al. [9]. The effect of different measurement ranges on the observed noise of a signal at ~25ºC is shown in figure 5. Naturally, the temperature fluctuations become large when the thermal camera's factory temperature range is increased from -40ºC-150ºC to 0ºC – 650ºC. When the signal is further attenuated using a reduced aperture, the temperature range becomes 0ºC – 1200ºC; however, the signal noise increases as well.
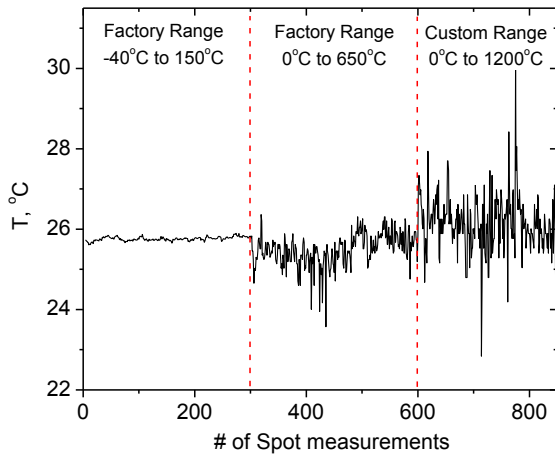

Fig. 5. *Effect of measurement range on observed noise.*

Table 1. NETD at different blackbody temperature setting for three camera temperature ranges.

T_{bb}	NETD		
	-40ºC to 150ºC	0ºC to 650ºC	0ºC to 1200ºC
ºC	ºC	ºC	ºC
25	0.036	0.346	0.783
50	0.033	0.298	0.834
100	0.024	0.220	0.654
450		0.101	0.395
600		0.060	0.256
750			0.258
900			0.212
1050			0.201
1200			0.192

While the NETD should scale with $\sim T^3$ over the full wavelength spectrum (*i.e.*, $\lambda \in \mathbb{R}^+$), for detectors that operate over finite spectral bands, the relationship between temperature and NETD is more complex. In this study with a microbolometer operating in the LW range, the NETD decreases exponentially with increasing temperatures as shown in figure 6. When the mean temperature is subtracted, the deviation from the average value of 25ºC, plotted in figure 7 for all three measurement ranges, follows a Gaussian profile with zero mean. Prior knowledge about the noise characteristics is valuable when designing noise mitigation strategies (figure 7).
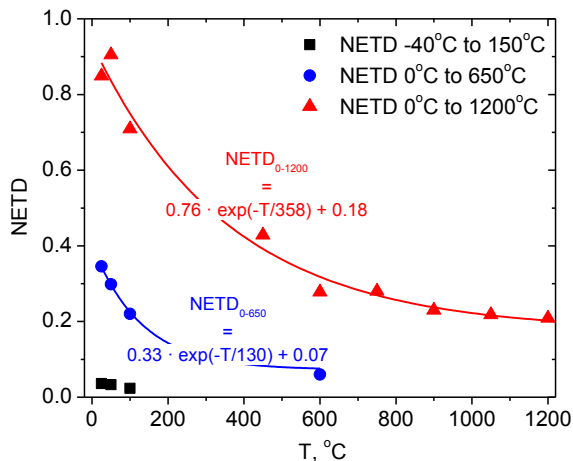

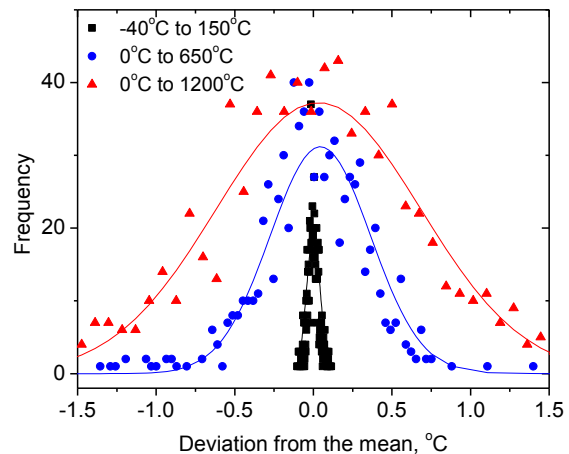**Fig. 6.** *NETD versus temperature (ºC) for the three measurement ranges.*

Fig. 7. *Deviation from the average temperature (25ºC) noise is Gaussian with zero mean.*

3. Noise mitigation techniques and IR image post processing

When dealing with thermographic images of warehouse fires, the high temperature range present within each image can cause difficulties when trying to find the optimum contrast adjustment. Even when using a non-linear colormap to an image, it is difficult to prevent local saturation or under-illumination, as shown in figures 8(a) and (b), respectively. When color-temperature information can be decoupled, local image contrast enhancement such as the Contrast-Limited Adaptive Histogram Equalization (CLAHE) algorithm can be used [11]. Rather than adjusting the whole image, the

CLAHE operates on small regions within the image called 'tiles'. Once each tile's contrast is enhanced, the tiles are combined using bilinear interpolation. The CLAHE algorithm can be very effective at showing object details at both high and low temperatures, as shown in figure 8(c). The downside of this technique, other than the fact that colors no longer represent specific temperatures, is the increase in observed noise levels in the low temperature regions. There are, however, tools available to mitigate the noise.
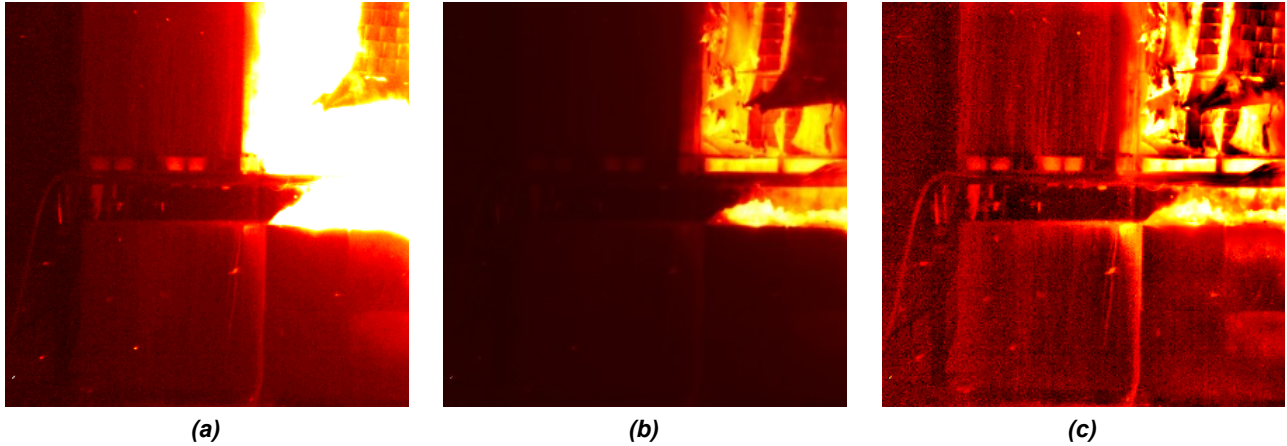

(a)   *(b)*   *(c)*

***Fig. 8.** Contrast adjustment favoring low temperatures (a), contrast adjustment favoring high temperatures (b), and contrast-limited adaptive histogram equalization (CLAHE) showing localized histogram adjustments (c). In figure (a) and (b), the color corresponds directly to a corresponding temperature. This temperature scale no longer has any meaning in figure (c).*

In case of thermographic imaging, noise is mostly caused by the finite Noise Equivalent Temperature Differences (NETDs) associated with the microbolometer array. The general tactic for image enhancement is to model the degradation and applying a subsequent inverse process. In general, image degradation can be due to an image degradation function, $h(x,y)$, and to additive noise, $\eta(x,y)$, so that

$$g(i,j) = h(i,j) \star f(i,j) + \eta(i,j) \tag{3}$$

In Eq. (3), *i* and *j* are the pixel coordinates, $h(i,j)$ is the degradation function (also called the point spread function), $\eta(i,j)$ is the additive noise, $f(i,j)$ is the noiseless input image, and $g(i,j)$ is the degraded image (as observed). The symbol '$\star$' indicates convolution.

The temperature setting of the SC655 microbolometer camera is controlled using different settings of the rolling shutter (factory) or, as described above and in [2], by placing a reduced aperture in front of the lens. Using a reduced aperture of 12.7 mm nearly doubles the F-number of the camera (f/1.0 to f/1.94). Since the depth of field increases with f-number, the degradation due to the point spread function, $h(i,j)$ should decrease. In other words, the aperture should cause the camera to focus over a greater depth. Furthermore, given that the subject distance is usually far away (> 20 m), the point spread function can be assumed to be the identity operator; therefore, image degradation due to the increased operational temperature range of the SC655 camera is purely caused by an additive noise component, *i.e.,* $\eta(i,j)$. In general, the more details are known about $\eta(i,j)$, the better $f(i,j)$ can be estimated. Given the above assumption with respect to the point spread function, for a sequence of images, Eq. (3) becomes

$$g(i,j) = f(i,j) + \eta(i,j) \tag{4}$$

Based on the analysis of the NETD in Section 2.2, the following characteristics are known about the noise component when the camera is in the 0°C – 1200°C range:
- The additive noise $\eta(i,j)$ is Gaussian in nature with a zero mean.
- The variance characterizing the Gaussian distribution reduces with increasing temperature (signal strength) and can be characterized by the following exponential decaying function (see figure 5):

$$NETD_{0-1200} = 0.76 \exp(-T/358) + 0.18 \tag{5}$$

Any filter used for IR image enhancement should be adaptive both with respect to the noise statistics as well as motion [10]. The motion in the images of interest stem from the movement of the flame as well as from burning or glowing embers flying through the image frame. Due to the motion, simple low-pass filters would result in image blurring and distortion of moving edges.

Two separate noise mitigating techniques are demonstrated in this study, namely:
- The Adaptive Kalman Filter (AKF)
- The Adaptive Median Filter (AMF)

In general, the Kalman filter is an algorithm that operates recursively on a series of measurements, containing noise, observed over time. The Kalman filter is commonly used for signal processing. In this work, a MATLAB version of the Kalman filter created by Campbell [14] was used. Campbell implemented a predictive Kalman-like filter in the time domain of the image stack based on the work by Mauer [15]. Algorithms for both the Adaptive Kalman Filter (AKF) and the Adaptive Median Filter (AMF) are shown in figures 9 and 10, respectively.

```
Input: G, V, ξ  Iₖ = Iₖ⁻ = Iₖ,  Eₖ⁻ = Eₖ

Loop k = 1:N
    Correction:
    Kₖ = Eₖ⁻/(Eₖ⁻ − V)
    Iₖ = GIₖ⁻ + (1 − G)Mₖ + Kₖ(Mₖ − Iₖ⁻)
    Eₖ = Eₖ⁻(1 − Kₖ)

    Adaptive mask:
    Γ = |Iₖ⁻−Mₖ|/√V  > ξ
    Iₖ(Γ) = Mₖ

    Prediction:
    Iₖ₊₁⁻ = Iₖ
    Eₖ₊₁⁻ = Eₖ

    Update:
    Eₖ⁻ = Eₖ₊₁⁻
    Iₖ⁻ = Iₖ₊₁⁻
end
```

Fig. 9. Adaptive Kalman filter used in this work.

```
Input: N

Loop k = -N:N
    A(i, j, k) = Mₖ(i, j)
end

I_med(i, j) = medianₖ[A(i, j, k)]
I_std(i, j) = Sdevₖ[A(i, j, k)]

ξ = Otsu[I_std(i, j)]
Γ = I_std(i, j) > ξ

I'ₖ(Γ) = Mₖ(Γ)
I'ₖ(Γᶜ) = I_med(Γᶜ)
```

Fig. 10. Adaptive median filer used in this work.

The AKF as used in this study is shown in pseudo code in figure 9 where G is the filter gain, V is the noise variance estimate (Eq. 5), I_k is the corrected image, I_k^- is the image prediction, E_k is the corrected variance estimate, E_k^- is the variance prediction, and K_k is the Kalman gain. In the adaptive component added to the algorithm for this work, Γ represents the mask, and ξ represents a threshhold. The mask assigns values of the current measurement to the corrected image when the current measurement deviates from the last prediction by more than ξ standard deviations. Here, ξ was set to 2.5 which gives approximately 99% confidence that the absolute difference at the same pixel location in I_k and M_k is not caused by random sensor noise.

The AMF (figure 10) applied in this study starts by creating an image stack, $A(i, j, k)$, i.e., $(2N + 1)$ deep. The standard deviation and the median of the image stack in the 'k' direction are calculated. Next, a threshold ξ, is determined by optimum global thresholding using Otsu's method [12] and the found standard deviation. The advantage of using this method is that it is free from any heuristics and based solely on the pixel information available. A mask, Γ, is created for pixels with a standard deviation that exceeds ξ. The pixels within the updated image are set to the current measured image when they fall within the mask. For all pixels that fall within the compliment of the mask, Γ^c, the value at pixel location $p(i,j)$ is set to the median of the image stack at the same pixel location.

The performance of the two filters is shown for a single pixel in figures 11 and 12. In this case, a pixel was chosen having a glowing ember flying by it, creating a distinct wavelet in the signal measurement. All temperature values were normalized for this example. Figure 12 shows that the impulse created by the burning ember only causes two pixel values to significantly deviate from the noisy background. The AKF as well as the AMF capture this wavelet since the deviation of these pixels compared to the prior pixel values greatly exceeds the threshold set for each method; forcing the filtered values to match the measurements. Using a regular Kalman filter (with gain G, set to 0.88) causes significant signal smearing; greatly underestimating the measured peak value of the flying ember.
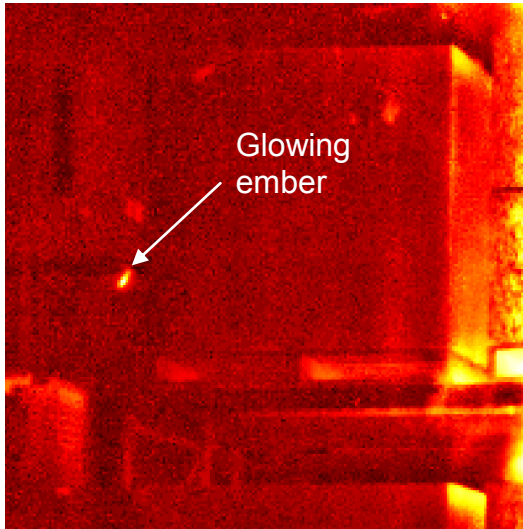
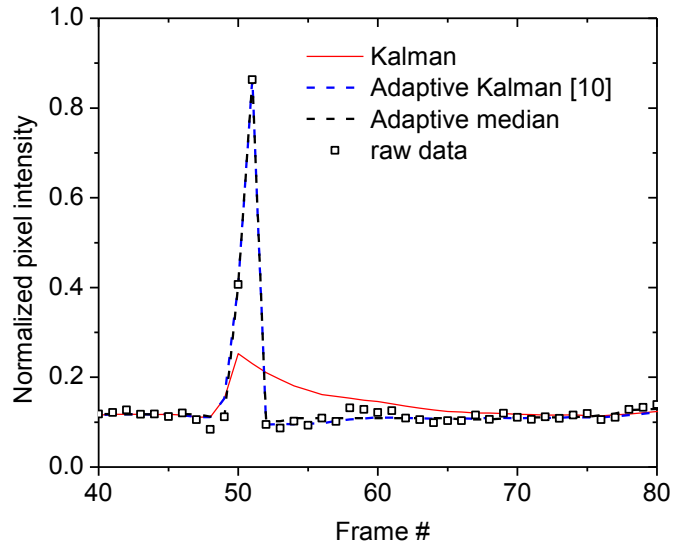**Fig. 11.** *Flying glowing ember in noisy image.*

Fig. 12. *Normalized pixel values at glowing ember location.*

The filters were applied to a particular thermograph image and the results are shown figures 13-16. Figure 13 shows the original thermograph after applying the CLAHE algorithm but without applying any noise filtering. The regular (non-adaptive) Kalman filter shows significant smearing effects (figure 14) where the movement of burning and glowing embers are 'smeared' in the spatial domain. When using the AKF, most of this smearing effect is reduced showing only faint trails following each ember (figure 15). Using the AMF (figure 16), the smearing is completely removed. Some of the smaller glowing pieces visible in the original image, however, were filtered out using the AMF.
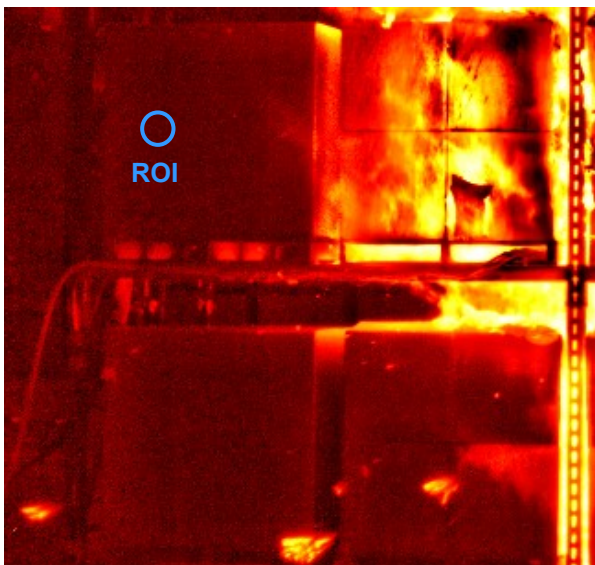

Fig. 13. *Original image after CLAHE no filter applied. Pixels inside the blue circle were used to estimate the noise in the spatial domain.*
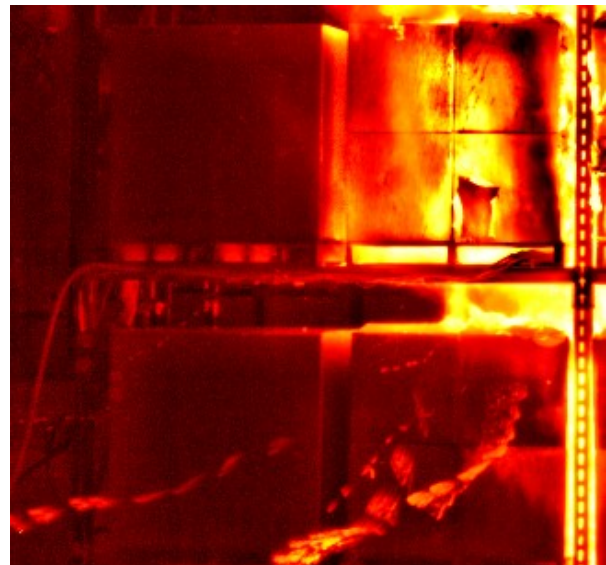

Fig. 14. *Regular Kalman filter with gain G set to 0.88. Significant signal smearing observed.*
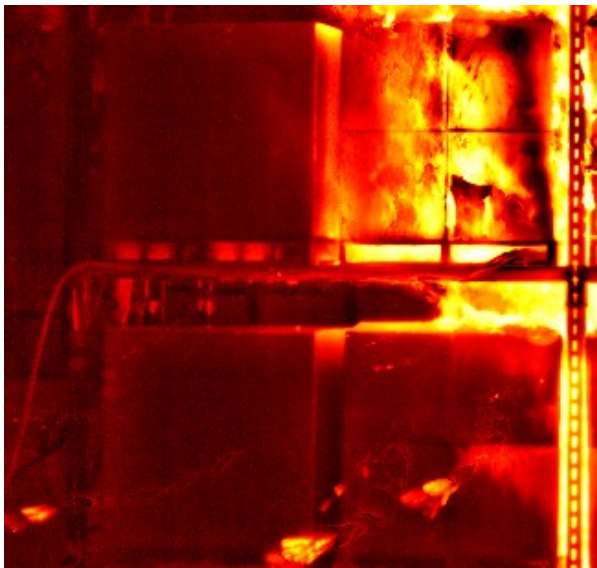
Fig. 15. *Adaptive Kalman filter. Much of the smearing effect removed.*

Fig. 16. *median filter over 16 frames.*

The spatial noise was measured by calculating the standard deviation of the pixels with the 174-pixel circular region of interest (ROI) shown in figure 13. For these images, the standard deviation in pixel noise within this ROI was reduced by 62% using the AMF and by 55% using the AKF. The effect of the filters is shown graphically in figures 17(a)-(c). Figure 17(a) shows the distribution of the noise (deviation around the mean) within the ROI shown in figure 13. Figure 17(b) shows the distribution from pixel residing within the same ROI after applying the adaptive Kalman filter. Finally, figure 17(c) shows the noise distribution after applying the adaptive median filter. The red curves in figures 17(a)-(c) represent a Gaussian fit through the data.
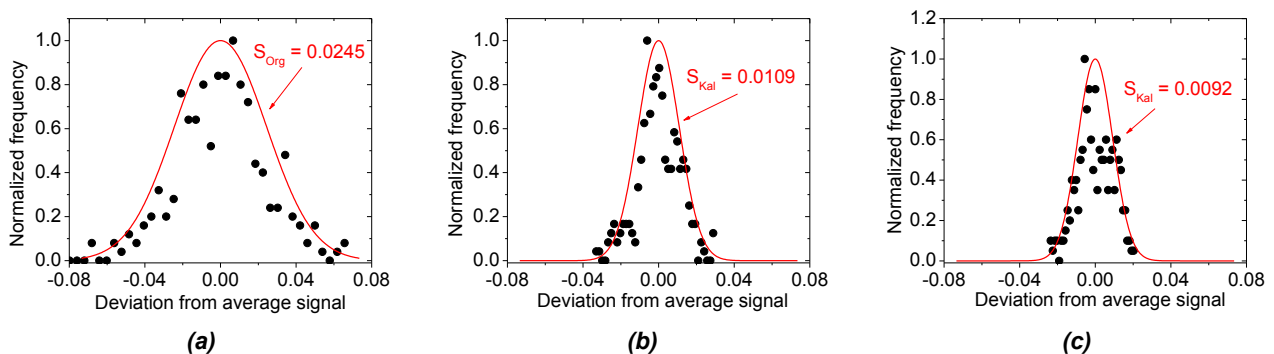

(a)

(b)

(c)

Fig. 17. *Results from histogram analysis with the region of interest represented by the blue circle in Fig. 13, for the original data (a), after applying the adaptive Kalman filter (b), and after applying the adaptive median filter (c).*

The two algorithms described only filter in the temporal domain. Due to its recursive nature, the AKF has the advantage of only requiring 'memorizing' two frames, the latest prediction and the latest correction. The AMF, however, requires a full $(2N + 1)$ stack to be placed in memory. This makes the AKF more likely to be applicable as a real time filter.

Overall, filtering high-temperature range, IR images obtained using an uncooled microbolometer, long-wavelength IR camera show significant noise improvement. The temperature noise characteristics at room temperature (~25ºC) after filtering an IR image with a temperature range set from 0ºC to 1200ºC are comparable to the noise characteristics of unfiltered images taken with the factory temperature setting of 0 ºC to 650ºC. Having a microbolometer camera capable of measuring temperatures ranging from room temperatures up to 1200ºC with low noise provides a valuable tool when studying warehouse fire dynamics.

4. Summary and conclusions

The effectiveness of using a high temperature range, microbolometer camera for the study of warehouse fire dynamics was investigated. The effect of applying a custom calibration on the observed noise equivalent temperature difference (NETD) was quantified. The pixel noise was found to be 'white' in nature, having a Gaussian distribution with zero mean. The NETD was shown to decay exponentially with increasing temperatures. The temperature-dependant noise information was used by two noise filtering algorithms; namely, an Adaptive Kalman Filter (AKF) and an Adaptive Median Filter (AMF). The 'adaptive' nature of these filters allowed capturing sudden rises and drops in temperature, which could be caused either by (flame) motion or by glowing embers flying through the field of view. The AKF and the AMF reduced the noise in the low temperature regime by 55% and 62%, respectively.

REFERENCES

[1] Gonzalez R.C., Woods R.E., Steven L.E., *Digital Image Processing* (2nd *ed*), Gatemark Publishing, 2009, p. 287.

[2] de Vries, "In Situ calibration of a microbolometer camera for the study of large-scale fires," Proc. SPIE 8705, Thermosense: Thermal Infrared Applications XL, 8705-1, April 30, 2013.

[3] Ditch B.D., "Flammability characterization of Li-ion batteries in bulk storage," Technical Report, FM Global, 2013, available at www.fmglobal.com/researchreports.

[4] de Vries, "Application of mid-wave and long-wave IR imaging in large-scale rack-storage fires," InfraMation 2013, Orlando FL, USA, ITC 2013-020, 2013.

[5] de Vries and B.D. Ditch, "Multi-spectral infrared analysis of Lithium-ion battery bulk-storage fire tests," 7th international Seminar on Fire and Explosion Hazards, Providence, RI, 5-10 May, 2013.

[6] Rajic, N., Rowlands, D., "Thermoelastic Stress Analysis with a Compact Low-Cost Microbolometer System," QIRT Journal, vol. 10, pp. 135-158, 2013

[7] Zukoski, E.E., "Properties of Fire Plumes," in Combustion Fundamental of Fire, (ed. G. Cox), pp. 101-219, Academic Press London, 1995.

[8] www.flir.com/thermography, (2012)

[9] Vollmer, M., Möllmann, K.-P., "Infrared Thermal Imaging," pp 139-142, Wiley-VCH verslag GmbH & Co., Wienheim, Germany, 2010.

[10] Reza, A.M., "Adaptive Noise Filtering of Image Sequences in Real Time," WSEAS Transactions on Systems, vol 12, pp. 189-201, 2013.

[11] Zuiderveld, K., "Contrast Limited Adaptive Histograph Equalization." *Graphic Gems IV*. San Diego: Academic Press Professional, 1994. 474–485.

[12] Otsu, N. "A Threshhold Selection Method from Gray Level Histograms," IEEE, Trans Systems, Man, and Cybernetics, vol. SMC-9, pp. 62-66, 1979.

[13] Kalman, R.E., "A new Approach to Linear Filerting and Prediction Problems," Transactions of the ASME– Journal of Basic Engineering, vol. 82, pp.35-45, 1960. (transcribed by John Lukesh)

[14] http://www.mathworks.com/matlabcentral/fileexchange/26334-kalman-filter-for-noisy-movies, visited 4/15/2014.

[15] http://rsb.info.nih.gov/ij/plugins/kalman.html, visited 4/15/204.